Magnetoelastic effects in the hyperhoneycomb Kitaev spin liquid

Aysel Shiralieva

Department of Physics, National Research University Higher School of Economics, Moscow, Russia

Artem Prokoshin

Lomonosov Moscow State University, Moscow 119991, Russia

Natalia B. Perkins

School of Physics and Astronomy, University of Minnesota, Minneapolis, Minnesota 55455, USA
E-mail: nperkins@umn.edu

In recent years, several magnetic Mott insulators with strong spin-orbit coupling were suggested to be proximate to the Kitaev quantum spin liquid, whose one of the most exciting features is the fractionalization of spin excitations into itinerant Majorana fermions and static Z_2 fluxes. Unfortunately, the ground states of these systems cannot be easily captured by experiment, remaining featureless to conventional local probes. Here we propose to study the signatures of fractionalized excitations by exploiting their coupling to the lattice vibrations, dubbed magnetoelastic coupling, which arises from the fact that the interaction between spins depends on the relative distance between them. We argue that the magnetoelastic coupling can lead to the distinct modification of the phonon dynamics, which can be observed by measuring renormalized phonon spectrum, the sound attenuation and the phonon Hall viscosity. This makes the phonon dynamics a promising tool for the characterization and identification of quantum spin liquid phases. In this work, we focus on the magnetoelastic effects in the three-dimensional Kitaev model realized on the hyperhoneycomb lattice. The hyperhoneycomb Kitaev spin liquid is particularly interesting since the strong Kitaev interaction was observed in the Kitaev magnet β-Li$_2$IrO$_3$, for which the spin-orbit entangled $J_{\text{eff}} = 1/2$ moments of iridium ions form precisely the hyperhoneycomb lattice*.

1. Introduction

Quantum spins in a solid can avoid a formation of long-range magnetic order even at zero temperature and instead can form a fluid type of the ground state. This state is known as a quantum spin liquid (QSL) and has a remarkable set of collective phenomena including topological ground-state degeneracy, long-range entanglement, and fractionalized excitations [1–7]. In recent years, much work has been done to understand the nature of QSL, however, even identifying realistic models which host this state is not a trivial task. In parallel, a long experimental quest has identified a number of two- and three-dimensional candidate materials belonging to the class of frustrated magnets, which provide evidence for spin liquid physics to exist in the real world [8–16].

When searching for QSL physics in real materials, a promising route is to look for signatures of spin fractionalizations in various types of dynamical probes, such as inelastic neutron scattering, Raman scattering, resonant inelastic x-ray scattering, ultrafast spectroscopy and terahertz nonlinear coherent spectroscopy, and thermodynamics [5–7, 15]. In addition, a lot of information can be obtained by studying the phonon dynamics in the QSL candidate materials [17–22], since the spin-lattice interaction is inevitable in real materials and is often rather strong [23–26]. The characteristic modifications of the phonon dynamics in QSL materials compared with their non-magnetic or magnetically ordered analogs can be observed in the renormalization of the spectrum of acoustic phonons [26], particular temperature dependence of the sound attenuation and the phonon Hall viscosity [19–21], the Fano line shapes of the Raman

Aysel Shiralieva, Artem Prokoshin, and Natalia B. Perkins

active phonons caused by the overlapping of the optical phonon modes with the continuum of the fractionalized excitations [22, 27–31], thermal conductivity and thermal Hall effect [24].

Particularly appealing is the possibility of using the phonon dynamics to probe spin fractionalization characteristic to the Kitaev spin liquid [32]. The Kitaev model is the prototypical example of a QSL model that possesses an exact solution. Introduced and solved by Alexei Kitaev in his seminal paper [32] on the honeycomb lattice, this model yet can be generalized and defined for various tri-coordinated three-dimensional (3D) lattices [33–40]. The Kitaev model describes a quantum spin-1/2 magnet and has a form

$$\mathcal{H}^s = -J^x \sum_{\langle \mathbf{r}, \mathbf{r}' \rangle \in x} \sigma_{\mathbf{r}}^x \sigma_{\mathbf{r}'}^x - J^y \sum_{\langle \mathbf{r}, \mathbf{r}' \rangle \in y} \sigma_{\mathbf{r}}^y \sigma_{\mathbf{r}'}^y - J^z \sum_{\langle \mathbf{r}, \mathbf{r}' \rangle \in z} \sigma_{\mathbf{r}}^z \sigma_{\mathbf{r}'}^z,$$

(1)

where $J^{x,y,z}$ are the coupling constants for the three types of bonds x, y, and z. In particular, spins fractionalize into two types of degrees of freedom in the Kitaev model: dispersing Majorana fermions (spinons) and gapped Z_2 fluxes. In the unperturbed Kitaev model, the flux is conserved, and the ground state can be viewed as a band insulator, or metal, of Majorana fermions in the flux background which minimizes the total energy. In the vicinity of the isotropic point, $J^x \sim J^y \sim J^z$, the ground state of both two-dimensional and three-dimensional Kitaev models has gapless Majorana fermions, which exhibit a rich variety of nodal structures, a systematic classification of which was done by O'Brien, *et al.* [35]. They found out that while the gapless QSLs in the hyperhoneycomb and the stripyhoneycomb are characterized by nodal lines of Dirac cones, Majorana fermion band structure on the hyperhexagon lattice has only bulk Weyls nodes [35]. On contrary, Majorana fermions on the hyperoctagon are characterized by a topological spinon Fermi surface [34].

The presence of exact solution makes the Kitaev spin liquids especially appealing because it gives a genuine opportunity for exploring QSL physics on a more quantitative level, since the response functions can be analytically computed for these special Hamiltonians [36–38, 40, 61–66]. These studies show that the nodal structures of the Majorana fermions in 2D and 3D Kitaev spin liquids leave unambiguous characteristic fingerprints in the dynamical probes. This is highly significant, because it gives us an opportunity to learn about generic behavior of other QSLs, which are much more difficult to describe. Another important aspect is that there exist suitable material candidates for realizing these Kitaev QSL phases [41, 42], such as the honeycomb iridates Na_2IrO_3 [43, 44] and α-Li_2IrO_3 [45], the honeycomb ruthenium chloride α-$RuCl_3$ [46, 47], and the 3D harmonic-honeycomb iridates β- and γ-Li_2IrO_3 [48–51]. Although all these candidate materials actually order at low temperature, the presence of a large Kitaev term suggests that these ordered ground states are proximate

to spin liquid phases — a statement which is also supported by recent experiments [16, 27, 52–60]. The comparison of the experimental findings with the available theoretical predictions allows us to understand how close are the candidate materials to their model counterparts.

In this paper, we focus on the study of the magnetoelastic effects in the Kitaev model on the hyperhoneycomb lattice. This is particularly important because of the existence of the Kitaev candidate material β-Li_2IrO_3 [48, 49], which is realized on the hyperhoneycomb lattice. While we know that other interactions are present in this compound in addition to the dominant Kitaev interaction, here we assume that some good intuition can be observed by studying the limiting case of the pure Kitaev model. The ground state of the isotropic Kitaev spin liquid on the hyperhoneycomb lattice corresponds to a fixed zero-flux configuration. This, however, can only be checked numerically, since the hyperhoneycomb lattice does not have any of the required mirror planes to apply Lieb's theorem [35, 67, 68]. Therefore, at temperatures below the flux gap Δ_{flux}, the low-energy magnetic excitations are solely dispersive Majorana fermions.

The main result presented in this paper is the derivation of the coupling vertices for the low-energy Majorana fermions and acoustic phonons. In order to obtain the Majorana fermion-phonon (MFPh) couplings, we performed a microscopic analysis of the change of the spin exchange energy due to the lattice distortion and obtain the explicit form of the MFPh couplings by considering acoustic phonon modes coupled to low-energy spin degrees of freedom expressed in terms of the Majorana fermions. We also found that in the low-energy limit, this coupling has essentially the same form as the one obtained from the symmetry considerations.

The knowledge of the MFPh couplings allows us to compute the phonon dynamics and, in particular, the experimentally observable consequences of the spin-lattice coupling such as phonon attenuation, phonon viscosity, phonon conductivity, and phonon Hall effect [20, 21]. Specifically, the sound attenuation may be measured by the ultrasound experiment and the Hall viscosity could be inferred from acoustic Faraday effect, thermal Hall effect and spectroscopy measurement.

The rest of the paper is organized as follows. In Sec. 2, we review the essential details and symmetry of the three-dimensional hyperhoneycomb lattice. In Sec. 3, we present the derivation of the spin-phonon Hamiltonian. In Sec. 3.1, we discuss the Kitaev model on the hyperhoneycomb lattice and obtain its fermionic band structure. We show that the fermions are gapless along the nodal line within the Γ-X-Y plane, for which we obtain an analytical equation. In 3.2, we introduce the lattice Hamiltonian for the acoustic phonons on the hyperhoneycomb lattice and obtain the acoustic phonon spectrum. In Sec. 3.3, we present the explicit microscopic derivation of the Majorana fermion-phonon coupling vertices and show that there are four symmetry channels which contribute into them. In Sec. 4, we present a short

summary and discuss the possibility for the spin fractionalization in the Kitaev hyperhoneycomb model to be seen in the phonon dynamics.

2. Brief review of the hyperhoneycomb structure

We start by reviewing essential details of the three-dimensional hyperhoneycomb lattice, which we sketch in Fig. 1. The hyperhoneycomb lattice is a face-centered orthorhombic lattice with four sites per primitive face-centered orthorhombic unit cell defined by the lattice vectors $\mathbf{a}_1 = (0, \sqrt{2}, 3)$, $\mathbf{a}_2 = (1, 0, 3)$, and $\mathbf{a}_3 = (1, \sqrt{2}, 0)$. The conventional orthorhombic unit cell is set by the crystallographic axes $\{\hat{\mathbf{a}}, \hat{\mathbf{b}}, \hat{\mathbf{c}}\}$, which are related to the Cartesian axes $\{\hat{\mathbf{x}}, \hat{\mathbf{y}}, \hat{\mathbf{z}}\}$ appearing in the spin Hamiltonian Eq. (1) by $\hat{\mathbf{x}} = (\hat{\mathbf{a}} + \hat{\mathbf{c}})/\sqrt{2}$, $\hat{\mathbf{y}} = (\hat{\mathbf{c}} - \hat{\mathbf{a}})/\sqrt{2}$, and $\hat{\mathbf{z}} = -\hat{\mathbf{b}}$. Different bond types x, y, and z are marked by red, green, and blue,
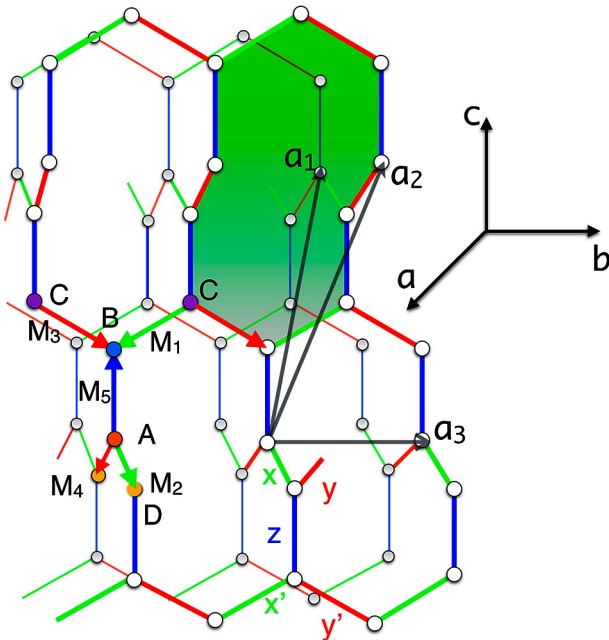

Fig. 1. (Color online) The sketch of the hyperhoneycomb lattice. The three lattice vectors of the primitive face-centered orthorhombic lattice are given by $\mathbf{a}_1 = (0, \sqrt{2}, 3)$, $\mathbf{a}_2 = (1, 0, 3)$, $\mathbf{a}_3 = (1, \sqrt{2}, 0)$. The four sublattices A, B, C, and D are shown, and we set $\mathbf{r}_A = (0, 0, 0)$. The nearest neighbor vectors are $\mathbf{M}_1 = \frac{1}{2}(1, \sqrt{2}, -1)$, $\mathbf{M}_2 = \frac{1}{2}(1, -\sqrt{2}, -1)$, $\mathbf{M}_3 = \frac{1}{2}(-1, -\sqrt{2}, -1)$, $\mathbf{M}_4 = \frac{1}{2}(-1, \sqrt{2}, -1)$, and $\mathbf{M}_5 = (0, 0, 1)$. Different bond types x, y, and z are marked by red, green, and blue, respectively. The conventional orthorhombic unit cell is set by the crystallographic axes $\hat{\mathbf{a}}$, $\hat{\mathbf{b}}$, and $\hat{\mathbf{c}}$, which are related to the Cartesian axes $\{\hat{\mathbf{x}}, \hat{\mathbf{y}}, \hat{\mathbf{z}}\}$ appearing in the spin Hamiltonian Eq. (1) by $\hat{\mathbf{x}} = (\hat{\mathbf{a}} + \hat{\mathbf{c}})/\sqrt{2}$, $\hat{\mathbf{y}} = (\hat{\mathbf{c}} - \hat{\mathbf{a}})/\sqrt{2}$, and $\hat{\mathbf{z}} = -\hat{\mathbf{b}}$. The shaded region denotes a loop on the hyperhoneycomb lattice containing 10 sites. The plaquette operator on such a loop is a conserved operator W_p, since $[W_p, \mathcal{H}_s] = 0$.

respectively. Note, however, that there are two non-equivalent types of x and y bonds, and the hyperhoneycomb structure can be viewed as a stacking of two types of zigzag chains formed by x and y, and x' and y' bonds run along two distinct directions (90° rotated with respect to each other): xy-chains run along $\mathbf{a} + \mathbf{b}$ direction and $x'y'$-chains run along $\mathbf{a} - \mathbf{b}$ direction. The two types of chains are interconnected with vertical z-bonds. Thus, in total, there are five types of nearest neighbor bonds: x, y, x', y', and z. Apart from translations, the crystal structure is invariant under the D_{2h} point group symmetry, which consists of (i). Inversion i through the center of every x- or y- or x'- or y'-type of bonds. (ii) Three π-rotations, $C_{2\mathbf{a}}$, $C_{2\mathbf{b}}$, and $C_{2\mathbf{c}}$, around the axes $\mathbf{a}$, $\mathbf{b}$, and $\mathbf{c}$, respectively, passing through the middle of the z bonds. In particular, $C_{2\mathbf{a}}$ maps x-bonds to y'-bonds and y-bonds to x'-bonds. Similarly, $C_{2\mathbf{b}}$ maps x-bonds to x'-bonds and y-bonds to y'-bonds. Finally, $C_{2\mathbf{c}}$ maps x-bonds to y-bonds and x'-bonds to y'-bonds. (iii) Three glide planes which arise by reflections across the **ab**-, **bc**- and **ac**-planes passing through an inversion center, followed by non-primitive translations by $(\frac{1}{4}\frac{1}{4}0)$, $(0\frac{1}{4}\frac{1}{4})$ and $(\frac{1}{4}0\frac{1}{4})$, in orthorhombic units, respectively.

3. The spin-phonon model

We focus our discussion on the spin-phonon Hamiltonian on the hyperhoneycomb lattice:

$$\mathcal{H} = \mathcal{H}^s + \mathcal{H}^{ph} + \mathcal{H}^c. \tag{2}$$

The *first term* in Eq. (2) is the spin Hamiltonian given by Eq. (1). The *second term* is the bare Hamiltonian for the acoustic phonons. The *third term* is the magnetoelastic coupling.

3.1. The Kitaev model on the hyperhoneycomb lattice

The spin Hamiltonian is given by Eq. (1). For simplicity, we consider the isotropic Kitaev model on the hyperhoneycomb lattice. Because only one component of the spin interacts along each bond, there is one conserved quantity for every plaquette, which on the hyperhoneycomb lattice consists of ten sites (see shaded region in Fig. 1). The plaquette operator is given by

$$\hat{W}_p = \prod_{\mathbf{r} \in P} \sigma_{\mathbf{r}}^{\alpha(\mathbf{r})}, \tag{3}$$

which is the product of spin operators around a plaquette P, whose spin component $\alpha(\mathbf{r})$ is given by the label of the outgoing bond direction. Since all plaquette operators $\hat{W}_p$ commute with the Hamiltonian and take eigenvalues of ± 1, the Hilbert space of the spin Hamiltonian $\mathcal{H}_s$ can be divided into eigenspaces of $\hat{W}_p$. The ground state of the Kitaev model on the hyperhoneycomb lattice is the zero-flux state

with all $W_p = 1$ [33, 35]. This, however, can not be shown exactly based on the Lieb's theorem [67] but only based on the numerical calculations [35, 40]. Thus, strictly speaking, the Kitaev model on hyperhoneycomb lattice is not exactly solvable.

Using the Kitaev fermionization $\sigma_{\mathbf{r}}^{\kappa} = i b_{\mathbf{r}}^{\kappa} c_{\mathbf{r}}$ with $\kappa = x, y, z$ [32], the spin Hamiltonian Eq. (1) can be rewritten as

$$\mathcal{H}^s = \sum_{\kappa} \sum_{\langle \mathbf{r}, \mathbf{r}' \rangle_{\kappa}} i J_{\kappa} \, u_{\mathbf{r}, \mathbf{r}'}^{\kappa} c_{\mathbf{r}} \, c_{\mathbf{r}'} = \frac{1}{2} \sum_{\mathbf{r}, \mathbf{r}'} \mathcal{H}_{\mathbf{r}, \mathbf{r}'} c_{\mathbf{r}} c_{\mathbf{r}'}, \quad (4)$$

where $u_{\mathbf{r}, \mathbf{r}'}^{\kappa} \equiv i b_{\mathbf{r}}^{\kappa} b_{\mathbf{r}'}^{\kappa} = \pm 1$, $\mathcal{H}_{\mathbf{r}, \mathbf{r}'} = i J_{\kappa} u_{\mathbf{r}, \mathbf{r}'}^{\kappa}$ if $\mathbf{r}$ and $\mathbf{r}'$ are neighboring sites connected by a κ bond and $\mathcal{H}_{\mathbf{r}, \mathbf{r}'} = 0$ otherwise. In the ground-state flux sector, we choose the gauge sector with all $u_{\mathbf{r}, \mathbf{r}'}^{\kappa} = 1$, which corresponds to all $W_p = 1$. The quadratic fermionic Hamiltonian in Eq. (4) can be diagonalized via a standard procedure [32]. Since the hyperhoneycomb lattice has four sites per unit cell, the resulting band structure has four fermion bands. The diagonal form of the Hamiltonian [38]

$$\mathcal{H}^s = \sum_{\mathbf{k}} \sum_{\mu=1}^{4} \varepsilon_{\mathbf{k}, \mu} \left[\psi_{\mathbf{k}, \mu}^{\dagger} \psi_{\mathbf{k}, \mu} - \frac{1}{2} \right] \quad (5)$$

is then obtained by the unitary transformation $\tilde{\mathcal{H}}_{\mathbf{k}} = \mathcal{W}_{\mathbf{k}} \cdot \mathcal{E}_{\mathbf{k}} \cdot \mathcal{W}_{\mathbf{k}}^{\dagger}$ of the Hermitian matrix $\tilde{\mathcal{H}}_{\mathbf{k}}$ with elements $(\tilde{\mathcal{H}}_{\mathbf{k}})_{\nu\nu'} = \frac{1}{N} \sum_{\mathbf{r} \in \nu} \sum_{\mathbf{r}' \in \nu'} \mathcal{H}_{\mathbf{r}, \mathbf{r}'} e^{i\mathbf{k} \cdot (\mathbf{r}' - \mathbf{r})}$, where $\varepsilon_{\mathbf{k}, \mu} = (\mathcal{E}_{\mathbf{k}})_{\mu\mu}$ are the fermion energies. The fermionic eigenmodes are given by

$$\psi_{\mathbf{k}, \mu} = \frac{1}{\sqrt{2N}} \sum_{\nu=1}^{n} \left(\mathcal{W}_{\mathbf{k}}^{\dagger} \right)_{\mu\nu} \sum_{\mathbf{r} \in \nu} c_{\mathbf{r}} \, e^{-i\mathbf{k} \cdot \mathbf{r}}. \quad (6)$$

Note that only the fermions $\psi_{\mathbf{k}, \mu}$ with energies $\varepsilon_{\mathbf{k}, \mu} > 0$ are physical due to the particle-hole redundancy $\tilde{\mathcal{H}}_{-\mathbf{k}} = -\tilde{\mathcal{H}}_{\mathbf{k}}^*$, which implies $\psi_{-\mathbf{k}, \mu} = \psi_{\mathbf{k}, \mu}^{\dagger}$ and $\varepsilon_{-\mathbf{k}, \mu} = -\varepsilon_{\mathbf{k}, \mu}$. Thus, only two branches will have positive spectrum. The lowest branch shown in Fig. 2 for the (k_a, k_b) plane exhibits the nodal line, which is protected by time-reversal symmetry [35]. We can also see that similarly to the spectrum of the Kitaev model on the honeycomb lattice, in this case, the dispersion is linear about the zero-energy modes, i.e., each point of the nodal line represents a Dirac cone. By solving the equation $\varepsilon_{\mathbf{k}, 1} = 0$, we obtained the functional form for the nodal line, which reads

$$k_b = \frac{1}{\sqrt{2}} \arg\left(1 - 2\cos k_a \pm i\sqrt{1 + 4\cos k_a - 2\cos 2k_a} \right). \quad (7)$$

In Fig. 3 we plot the density of states (DOS) for the hyperhoneycomb Kitaev model (shown by the black line). The DOS is defined as

$$\text{DOS}(E) = \sum_{\mu=1,2} \int_{BZ} \delta(E - \epsilon_{\mathbf{k}, \mu}) d^3 \mathbf{k}, \quad (8)$$
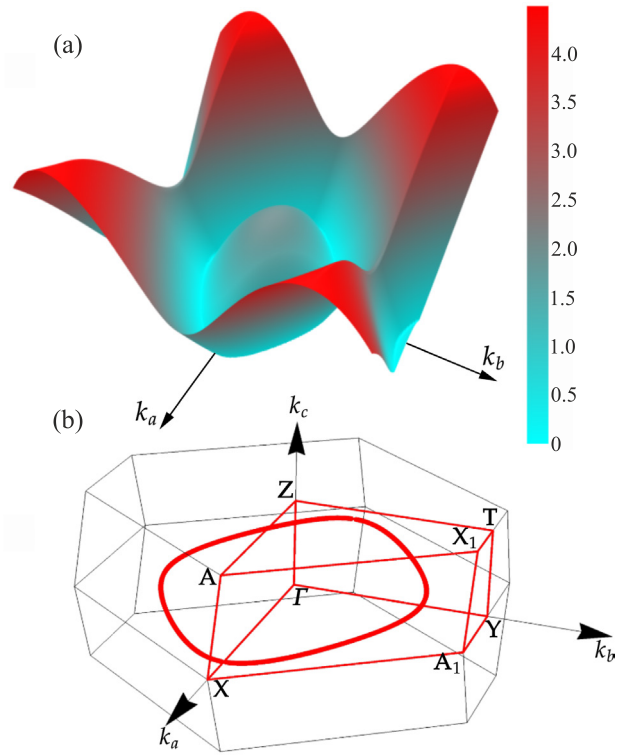

Fig. 2. (Color online) Panel (a) shows the dispersion of the lowest branch of the fermionic excitations in the hyperhoneycomb Kitaev model through the plane of the nodal line, whose position in the Brillouin zone is explicitly shown in panel (b).

where the contributions from both branches of excitations are summed up. The low-energy density of states is linear in energy, which follows directly from the linear low-energy dispersion and the dimension of the Fermi surface, d_f, or in other words, the dimension of the set of points on which the energy is zero — for a nodal line $d_f = 1$ and for a Dirac point $d_f = 0$ [36]. For comparison, in Fig. 3 we also plot the DOS for the 2D honeycomb model (shown by the red line). The differences between the densities of states for these two lattices can be understood in terms of the
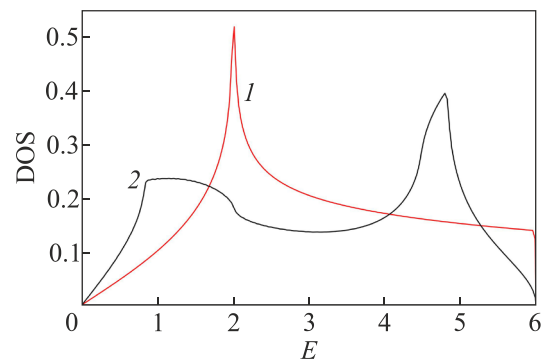

Fig. 3. (Color online) One-fermion densities of states of isotropic Kitaev models on the honeycomb (red line, *1*) and hyperhoneycomb (black line, *2*) lattices. In each case, the density of states is normalized such that its integral is unity.

number of fermionic bands, one for the honeycomb lattice and two for the hyperhoneycomb lattices, and their nodal structure — two Dirac points for the honeycomb lattice and the closed line of Dirac points for the hyperhoneycomb lattice. The former leads to the absence of the Van Hove singularities and overall more flatten DOS for the hyperhoneycomb lattice. The latter is responsible for a faster growth of the hyperhoneycomb DOS at low energies, which is consistent with higher dimensionality of the nodal line and enlarged number of low-energy states.

3.2. Acoustic phonons on the hyperhoneycomb lattice

The bare Hamiltonian for the acoustic phonons on the hyperhoneycomb lattice is given by

$$\mathcal{H}_{ph} = \mathcal{H}_{ph}^{kinetic} + \mathcal{H}_{ph}^{elastic} \qquad (9)$$

Here, $\mathcal{H}_{ph}^{kinetic} = \sum_{\mathbf{q},\mu} \dfrac{\mathbf{P}_{-\mathbf{q},\mu} \cdot \mathbf{P}_{\mathbf{q},\mu}}{2\rho\delta_V}$, where $\mathbf{P}_{\mathbf{q},\mu}$ is the momentum of the phonon with polarization μ, δ_V is the area enclosed in one unit cell and ρ is the mass density of the lattice ions.

In order to describe the dynamics of the low-energy acoustic phonons, it is convenient to move away from the Hamiltonian formulation and employ instead the long-wavelength effective action $\mathcal{S}$ approach in terms of the fields $\mathbf{u} = \{u_a, u_b, u_c\}$, which describe the displacement of an atom from its original location. To lowest order, it reads [69]

$$\mathcal{S}_{ph}^{(s)} = \int d^2 x d\tau \Big[\rho(\partial_\tau \mathbf{u})^2 + F \Big], \quad F = \frac{1}{2}\mathcal{C}_{ijlk}\epsilon_{ij}\epsilon_{lk}, \quad (10)$$

where F is the elastic free energy, $\epsilon_{ij} = \dfrac{1}{2}(\partial_i u_j + \partial_j u_i)$ are the components of the strain tensor and C_{ijlk} represent the elements of the elastic modulus tensor. From symmetry considerations, for a lattice with D_{2h} point group symmetry, there are nine independent non-zero elastic modulus tensor coefficients: C_{aaaa}, C_{bbbb}, C_{cccc}, C_{acac}, C_{abab}, C_{aabb}, C_{aacc}, C_{bbcc}, C_{bcbc}. Performing the Fourier transform, $\mathbf{u}(\mathbf{r}) = \dfrac{1}{\sqrt{N}}\sum_{\mathbf{q}} e^{i\mathbf{q}\mathbf{r}}\mathbf{u}_{\mathbf{q}}$, the elastic free energy can be explicitly written as

$$F = \frac{1}{2}\begin{pmatrix} C_{aaaa}q_a^2 + C_{acac}q_c^2 + C_{abab}q_b^2 & q_b q_a (C_{aabb} + C_{abab}) & q_a q_c (C_{aacc} + C_{acac}) \\ q_b q_a (C_{aabb} + C_{abab}) & C_{abab}q_a^2 + C_{bcbc}q_c^2 + C_{bbbb}q_b^2 & q_b q_c (C_{bbcc} + C_{bcbc}) \\ q_a q_c (C_{aacc} + C_{acac}) & q_b q_c (C_{bbcc} + C_{bcbc}) & C_{acac}q_a^2 + C_{cccc}q_c^2 + C_{bcbc}q_b^2 \end{pmatrix}, \qquad (11)$$

where $q_a = q\sin\theta\cos\phi$, $q_b = q\sin\theta\sin\phi$ and $q_c = q\cos\theta$ are the components of the acoustic vector $\mathbf{q}$ in the orthorhombic reference frame. By diagonalizing the matrix (11), we compute eigenmodes, one longitudinal and two transverse acoustic modes, and the corresponding eigenenergies. The longitudinal and transverse acoustic phonons are then given by

$$\begin{pmatrix} u_{\mathbf{q},a} \\ u_{\mathbf{q},b} \\ u_{\mathbf{q},c} \end{pmatrix} = \begin{pmatrix} R_{11}(\theta,\phi) & R_{12}(\theta,\phi) & R_{13}(\theta,\phi) \\ R_{21}(\theta,\phi) & R_{22}(\theta,\phi) & R_{23}(\theta,\phi) \\ R_{31}(\theta,\phi) & R_{32}(\theta,\phi) & R_{33}(\theta,\phi) \end{pmatrix}\begin{pmatrix} \tilde{u}_{\mathbf{q}}^{\parallel} \\ \tilde{u}_{\mathbf{q}}^{1,\perp} \\ \tilde{u}_{\mathbf{q}}^{2,\perp} \end{pmatrix}, \quad (12)$$

where $\hat{R}$ is the transformation matrix. The energies of the longitudinal and transverse acoustic phonons are

$$\Omega_{\mathbf{q}}^{\parallel} = v_s^{\parallel}(\theta,\phi)q,$$
$$\Omega_{\mathbf{q}}^{1,\perp} = v_s^{1,\perp}(\theta,\phi)q, \qquad (13)$$
$$\Omega_{\mathbf{q}}^{2,\perp} = v_s^{2,\perp}(\theta,\phi)q,$$

where the sound velocities for the longitudinal acoustic mode, $v_s^{\parallel}(\theta,\phi)$, and two transverse modes, $v_s^{1,\perp}(\theta,\phi)$ and $v_s^{2,\perp}(\theta,\phi)$ are anisotropic in space. In Fig. 4, we plot the angular dependences of these velocities computed for the elastic modulus tensor coefficients close to those in β-LiIr$_2$O$_3$ (in kbar): $C_{aaaa} = C_{bbbb} = C_{cccc} = 2800$, $C_{aacc} = C_{bbcc} = 1300$, $C_{aabb} = C_{abab} = C_{acac} = C_{bcbc} = 900$ [70], such that the maximum velocity is set to $2\cdot10^4$ m/s, which is close to $v_s^{\parallel}$ in α-RuCl$_3$ estimated from the Debye temperature [20].
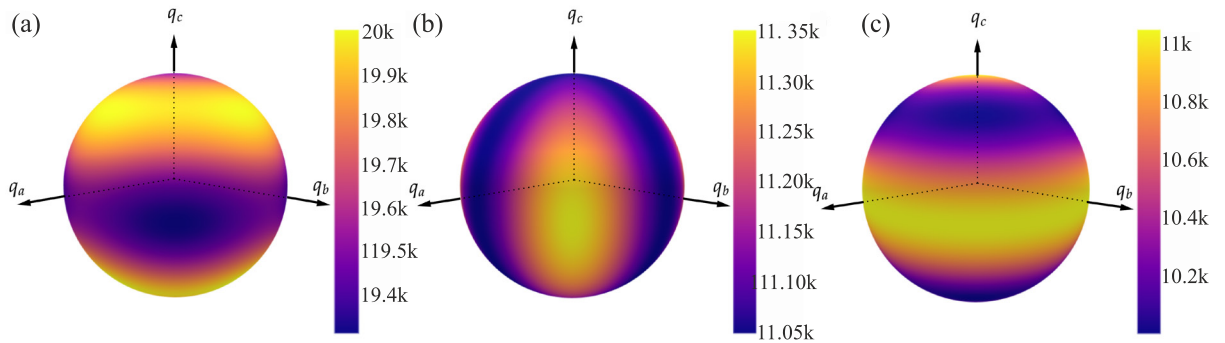

Fig. 4. Angular dependence of the sound velocities for (a) longitudinal mode and (b), and (c) two transverse modes.

Knowing the acoustic phonon dispersion relations, we can now determine the free phonon propagator in terms of lattice displacement field $\tilde{u}_{\mathbf{q}}^{\nu}$ is given by

$$D_{\nu\nu,\mathbf{q}}^{(0)}(t) = -i\langle T\tilde{u}_{-\mathbf{q}}^{\nu}(t)\tilde{u}_{\mathbf{q}}^{\nu}(0)\rangle^{(0)}, \qquad (14)$$

where T is time ordering operator, the superscript (0) denotes the bare propagator, $\nu = \|, (1, \perp), (2, \perp)$ labels the polarization, and $\tilde{u}_{\mathbf{q}}^{\nu}$ are phonon eigenmodes in the corresponding polarizations. We follow the convention in Ashcroft and Mermin [71], and write the second quantized form of $\tilde{u}_{\mathbf{q}}^{\nu}$ as

$$\tilde{u}_{\mathbf{q}}^{\nu}(t) = i(\frac{\hbar}{2\rho\delta_V\Omega_{\mathbf{q}}^{\nu}})^{1/2}(\tilde{a}_{\mathbf{q}}e^{-i\Omega_{\mathbf{q}}^{\nu}t} + \tilde{a}_{-\mathbf{q}}^{\dagger}e^{i\Omega_{\mathbf{q}}^{\nu}t}), \qquad (15)$$

where δ_V is the area enclosed in one unit cell and ρ is the mass density of the lattice ions. The time-ordered phonon propagator in the momentum and frequency space is then given by

$$D_{\nu\nu}^{(0)}(\mathbf{q},\Omega) = \int dt D_{\nu\nu,\mathbf{q}}^{(0)}(t)e^{i\Omega t} = -\frac{\hbar}{\rho\delta_V}\frac{1}{\Omega^2 - (\Omega_{\mathbf{q}}^{\nu})^2 + i\delta}. \qquad (16)$$

The dynamics of phonons will be thus described by the decay and scattering of these eigenmodes on low-energy fractionalized excitations of the Kitaev model, which can be accounted for by the phonon self-energy. At the lowest order, the phonon self-energy is given by the polarization bubble that can be expressed as [20]:

$$\Pi_{\text{ph}}^{\nu\nu'}(\mathbf{q},\Omega) = \frac{-i}{2!}\int dt e^{i\Omega t}\frac{1}{N}\sum_{\mathbf{k},\mathbf{k'}}\left\langle T\psi_{-\mathbf{k}-\mathbf{q}}^T(t)\hat{\lambda}_{\mathbf{q},\mathbf{k}}^{\nu}\psi_{\mathbf{k}}(t)\psi_{-\mathbf{k'}+\mathbf{q}}^T(0)\hat{\lambda}_{-\mathbf{q},\mathbf{k'}}^{\nu'}\psi_{\mathbf{k'}}(0)\right\rangle = i\text{Tr}\left[\hat{\lambda}_{\mathbf{q},\mathbf{k}}^{\nu}\mathcal{G}(\mathbf{k},\omega)\hat{\lambda}_{\mathbf{q},\mathbf{k}}^{\nu'}\mathcal{G}(\mathbf{k}-\mathbf{q},\omega+\Omega)\right], \qquad (17)$$

where $\nu, \nu' = \|, (1, \perp), (2, \perp)$ and $\mathcal{G}(\mathbf{k},\omega)$ denotes the Majorana fermions Green's function for the lowest branch, i.e., given by $\psi_{\mathbf{k}} \equiv \psi_{\mathbf{k},1}$, which is given by

$$\mathcal{G}(\mathbf{k},\omega) = -i\int_{-\infty}^{+\infty}dt\left\langle T\psi_{\mathbf{k}}(t)\psi_{-\mathbf{k}}^T(0)\right\rangle e^{i\omega t}, \qquad (18)$$

and $\hat{\lambda}_{\mathbf{q},\mathbf{k}}^{\nu}$ are the Majorana fermion-phonon (MFPh) coupling vertices. The renormalized phonon propagator is then given by the equation

$$D(\mathbf{q},\Omega) = \left\{\left(D^{(0)}(\mathbf{q},\Omega)\right)^{-1} - \Pi_{\text{ph}}(\mathbf{q},\Omega)\right\}^{-1}. \qquad (19)$$

Thus, in order to study the phonon dynamics in the Kitaev spin liquid, it remains to compute the MFPh coupling vertices $\hat{\lambda}_{\mathbf{q},\mathbf{k}}^{\nu}$, which we will do in the next section.

3.3. Microscopic derivation of the effective low-energy coupling Hamiltonian

The *third term* in Eq. (2) denotes the magneto-elastic coupling that arises from the change in the Kitaev coupling due to the lattice vibrations. In this section, we express the spin-lattice coupling in terms of the MFPh coupling and derive the explicit expressions for the MFPh coupling vertices. This is the main result of this work.

In the long wavelength limit for the acoustic phonons, the coupling Hamiltonian on the bond can be written in a differential form:

$$\mathcal{H}_{\mathbf{r},\mathbf{r}+\mathbf{M}_{\alpha}}^c = -\lambda\mathbf{M}_{\alpha}\cdot\left(\mathbf{u}(\mathbf{r}) - \mathbf{u}(\mathbf{r}+\mathbf{M}_{\alpha})\right)\sigma_{\mathbf{r}}^{\alpha}\sigma_{\mathbf{r}+\mathbf{M}_{\alpha}}^{\alpha} =$$
$$= \lambda\mathbf{M}_{\alpha}\cdot\left[\left(\mathbf{M}_{\alpha}\cdot\nabla\right)\mathbf{u}(\mathbf{r})\right]\sigma_{\mathbf{r}}^{\alpha}\sigma_{\mathbf{r}+\mathbf{M}_{\alpha}}^{\alpha}, \qquad (20)$$

where $\lambda \sim \left(\dfrac{dJ}{dr}\right)_{\text{eq}}l_a$ is the strength of the spin-phonon interaction and l_a is the lattice constant. On the hyperhoneycomb lattice, there are five inequivalent nearest neighbor $x, y, z, x'y'$ bonds, defined, respectively, by $\mathbf{M}_{\alpha} = (\mathbf{M}_1, \mathbf{M}_2, \mathbf{M}_3, \mathbf{M}_4, \mathbf{M}_5)$ (see Fig. 1) given by

$$\mathbf{M}_1 = \frac{1}{2}\left(1,\sqrt{2},-1\right), \quad \mathbf{M}_2 = \frac{1}{2}\left(1,-\sqrt{2},-1\right),$$
$$\mathbf{M}_3 = \frac{1}{2}\left(-1,\sqrt{2},-1\right), \quad \mathbf{M}_4 = \frac{1}{2}\left(-1,\sqrt{2},-1\right),$$
$$\mathbf{M}_5 = \left(0,0,1\right), \qquad (21)$$

where all the components of these vectors are given in the orthorhombic coordinates and are shown in Fig. 1. Note also that we choose the directions of $\mathbf{M}_i$ vectors such that the zero-flux ground state sector corresponds to $u_{ij} = 1$ in all nearest neighbor bonds when $i \in A$ and $i \in B$. Using these vectors, we can write the spin-phonon coupling Hamiltonian as

$$\mathcal{H} = \frac{1}{4}\lambda\sum_{r_A}\Big[4\sigma_{\mathbf{r}_A}^z\sigma_{\mathbf{r}_A+\mathbf{M}_5}^z\epsilon_{cc} +$$

$$+ \sigma_{\mathbf{r}_A}^y\sigma_{\mathbf{r}_A+\mathbf{M}_2}^y\left(\epsilon_{aa} + 2\epsilon_{bb} + \epsilon_{cc} - 2\sqrt{2}\epsilon_{ab} - 2\epsilon_{ac} + 2\sqrt{2}\epsilon_{bc}\right) + \sigma_{\mathbf{r}_A}^x\sigma_{\mathbf{r}_A+\mathbf{M}_4}^x\left(\epsilon_{aa} + 2\epsilon_{bb} + \epsilon_{cc} - 2\sqrt{2}\epsilon_{ab} + 2\epsilon_{ac} - 2\sqrt{2}\epsilon_{bc}\right)\Big] +$$

$$+ \sum_{r_B}\Big[\sigma_{\mathbf{r}_B}^y\sigma_{\mathbf{r}_B+\mathbf{M}_1}^y\left(\epsilon_{aa} + 2\epsilon_{bb} + \epsilon_{cc} + 2\sqrt{2}\epsilon_{ab} - 2\epsilon_{ac} - 2\sqrt{2}\epsilon_{bc}\right) + \sigma_{\mathbf{r}_B}^x\sigma_{\mathbf{r}_B+\mathbf{M}_3}^x\left(\epsilon_{aa} + 2\epsilon_{bb} + \epsilon_{cc} + 2\sqrt{2}\epsilon_{ab} + 2\epsilon_{ac} + 2\sqrt{2}\epsilon_{bc}\right)\Big]. \qquad (22)$$

In the following, we follow the symmetry arguments to write down the spin-phonon Hamiltonian, which will have four independent symmetry channels under D_{2h}, i.e., A_g, B_{1g}, B_{2g}, and B_{3g}, which are the inversion-symmetric irreducible representations (IRRs) of this group. The linear combinations of the strain tensors that transform as the D_{2h} are ϵ_{aa}, ϵ_{bb}, and ϵ_{cc}, in the A_g channel, and ϵ_{ab}, ϵ_{ac}, and ϵ_{bc} in B_{1g}, B_{2g}, and B_{3g}, respectively. Then we identify the linear combinations of the Kitaev interactions that transform according to these IRRs. To do this, we need to remember that the symmetry of the Kitaev model (1) involves combined lattice and spin transformations. In particular, the three π-rotations around the crystallographic axes $\mathbf{a}$, $\mathbf{b}$, and $\mathbf{c}$ must be combined with the rotations in the spin space: $C_{2\mathbf{a}}$ rotation should be combined with $[\sigma_x, \sigma_y, \sigma_z] \rightarrow [-\sigma_y, -\sigma_x, -\sigma_z]$ transformation in spin space; similarly, $C_{2\mathbf{b}}$ with $[\sigma_x, \sigma_y, \sigma_z] \rightarrow [-\sigma_x, -\sigma_y, \sigma_z]$

and $C_{2\mathbf{c}}$ with $[\sigma_x, \sigma_y, \sigma_z] \rightarrow [\sigma_y, \sigma_x, -\sigma_z]$ rotations in spin space. Taking this into account, we find

$$A_g^{\text{sp}} \sim (\sigma_{\mathbf{r_A}}^z \sigma_{\mathbf{r_A}+\mathbf{M_5}}^z,$$

$$\sigma_{\mathbf{r_B}}^y \sigma_{\mathbf{r_B}+\mathbf{M_1}}^y + \sigma_{\mathbf{r_A}}^y \sigma_{\mathbf{r_A}+\mathbf{M_2}}^y + \sigma_{\mathbf{r_B}}^x \sigma_{\mathbf{r_B}+\mathbf{M_3}}^x + \sigma_{\mathbf{r_A}}^y \sigma_{\mathbf{r_A}+\mathbf{M_4}}^y),$$

$$B_{1g}^{\text{sp}} \sim \sigma_{\mathbf{r_B}}^y \sigma_{\mathbf{r_B}+\mathbf{M_1}}^y - \sigma_{\mathbf{r_A}}^y \sigma_{\mathbf{r_A}+\mathbf{M_2}}^y + \sigma_{\mathbf{r_B}}^x \sigma_{\mathbf{r_B}+\mathbf{M_3}}^x - \sigma_{\mathbf{r_A}}^x \sigma_{\mathbf{r_A}+\mathbf{M_4}}^x,$$

$$B_{2g}^{\text{sp}} \sim -\sigma_{\mathbf{r_B}}^y \sigma_{\mathbf{r_B}+\mathbf{M_1}}^y - \sigma_{\mathbf{r_A}}^y \sigma_{\mathbf{r_A}+\mathbf{M_2}}^y + \sigma_{\mathbf{r_B}}^x \sigma_{\mathbf{r_B}+\mathbf{M_3}}^x + \sigma_{\mathbf{r_A}}^x \sigma_{\mathbf{r_A}+\mathbf{M_4}}^x,$$

$$B_{3g}^{\text{sp}} \sim -\sigma_{\mathbf{r_B}}^y \sigma_{\mathbf{r_B}+\mathbf{M_1}}^y + \sigma_{\mathbf{r_A}}^y \sigma_{\mathbf{r_A}+\mathbf{M_2}}^y + \sigma_{\mathbf{r_B}}^x \sigma_{\mathbf{r_B}+\mathbf{M_3}}^x - \sigma_{\mathbf{r_A}}^x \sigma_{\mathbf{r_A}+\mathbf{M_4}}^x.$$

The spin-phonon coupling Hamiltonian $\mathcal{H}_c$ can be written as a sum of four independent contributions, one from $A_g^{\text{ph}} \otimes A_g^{\text{sp}}$ and three from $B_{1g}^{\text{ph}} \otimes B_{1g}^{\text{sp}}$, $B_{2g}^{\text{ph}} \otimes B_{2g}^{\text{sp}}$ and $B_{3g}^{\text{ph}} \otimes B_{3g}^{\text{sp}}$. Thus, $\mathcal{H}_c = \mathcal{H}_c^{A_g} + \mathcal{H}_c^{B_{1g}} + \mathcal{H}_c^{B_{2g}} + \mathcal{H}_c^{B_{3g}}$, where:

$$\mathcal{H}_c^{A_g} = \lambda_{A_g} \sum_{\mathbf{r_A},\mathbf{r_B}} \left\{ 4\epsilon_{cc}\sigma_{\mathbf{r_A}}^z \sigma_{\mathbf{r_A}+\mathbf{M_5}}^z + (\epsilon_{aa} + 2\epsilon_{bb} + \epsilon_{cc})\left(\sigma_{\mathbf{r_B}}^y \sigma_{\mathbf{r_B}+\mathbf{M_1}}^y + \sigma_{\mathbf{r_A}}^y \sigma_{\mathbf{r_A}+\mathbf{M_2}}^y + \sigma_{\mathbf{r_B}}^x \sigma_{\mathbf{r_B}+\mathbf{M_3}}^x + \sigma_{\mathbf{r_A}}^x \sigma_{\mathbf{r_A}+\mathbf{M_4}}^x\right)\right\},$$

$$\mathcal{H}_c^{B_{1g}} = \lambda_{B_{1g}} \sum_{\mathbf{r_A},\mathbf{r_B}} \epsilon_{ab} \left(\sigma_{\mathbf{r_B}}^y \sigma_{\mathbf{r_B}+\mathbf{M_1}}^y - \sigma_{\mathbf{r_A}}^y \sigma_{\mathbf{r_A}+\mathbf{M_2}}^y + \sigma_{\mathbf{r_B}}^x \sigma_{\mathbf{r_B}+\mathbf{M_3}}^x - \sigma_{\mathbf{r_A}}^x \sigma_{\mathbf{r_A}+\mathbf{M_4}}^x\right),$$

$$\mathcal{H}_c^{B_{2g}} = \lambda_{B_{2g}} \sum_{\mathbf{r_A},\mathbf{r_B}} \epsilon_{ac} \left(-\sigma_{\mathbf{r_B}}^y \sigma_{\mathbf{r_B}+\mathbf{M_1}}^y - \sigma_{\mathbf{r_A}}^y \sigma_{\mathbf{r_A}+\mathbf{M_2}}^y + \sigma_{\mathbf{r_B}}^x \sigma_{\mathbf{r_B}+\mathbf{M_3}}^x + \sigma_{\mathbf{r_A}}^x \sigma_{\mathbf{r_A}+\mathbf{M_4}}^x\right), \quad (23)$$

$$\mathcal{H}_c^{B_{3g}} = \lambda_{B_{3g}} \sum_{\mathbf{r_A},\mathbf{r_B}} \epsilon_{bc} \left(-\sigma_{\mathbf{r_B}}^y \sigma_{\mathbf{r_B}+\mathbf{M_1}}^y + \sigma_{\mathbf{r_A}}^y \sigma_{\mathbf{r_A}+\mathbf{M_2}}^y + \sigma_{\mathbf{r_B}}^x \sigma_{\mathbf{r_B}+\mathbf{M_3}}^x - \sigma_{\mathbf{r_A}}^x \sigma_{\mathbf{r_A}+\mathbf{M_4}}^x\right),$$

where we absorbed numerical prefactors into the definitions of the coupling constants λ_{A_g}, $\lambda_{B_{1g}}$, $\lambda_{B_{2g}}$ and $\lambda_{B_{3g}}$.

Next, we express the spin-lattice coupling in terms of the MFPh coupling. To this end, we again express the spin operators in terms of the Majorana fermions using $\sigma_{\mathbf{r}}^\kappa = i b_{\mathbf{r}}^\kappa c_{\mathbf{r}}$. Performing the Fourier transformation of the

Majorana fermions given by $c_{\mathbf{r},\alpha} = \sqrt{\dfrac{2}{N}}\sum_{\mathbf{k}} c_{\mathbf{k},\alpha} e^{i\mathbf{k}\cdot\mathbf{r}_\alpha}$, where $\alpha = A, B, C, D$, we rewrite the product of the spin variables in terms of the Majorana fermions on all inequivalent bonds as

$$\sigma_{\mathbf{r}}^y \sigma_{\mathbf{r}+\mathbf{M_1}}^y \rightarrow \mathbf{A}_{-\mathbf{q}-\mathbf{k}}^{\mathbf{T}} \mathbf{S}_{\mathbf{k}}^\dagger \begin{pmatrix} 0 & -ie^{i\mathbf{k}\cdot\mathbf{a}_3} & 0 & 0 \\ ie^{-i\mathbf{k}\cdot\mathbf{a}_3} & 0 & 0 & 0 \\ 0 & 0 & 0 & 0 \\ 0 & 0 & 0 & 0 \end{pmatrix} \mathbf{S}_{\mathbf{k}} \mathbf{A}_{\mathbf{k}}, \quad \sigma_{\mathbf{r}}^y \sigma_{\mathbf{r}+\mathbf{M_2}}^y \rightarrow \mathbf{A}_{-\mathbf{q}-\mathbf{k}}^{\mathbf{T}} \mathbf{S}_{\mathbf{k}}^\dagger \begin{pmatrix} 0 & 0 & 0 & 0 \\ 0 & 0 & 0 & 0 \\ 0 & 0 & 0 & ie^{i\mathbf{k}\cdot\mathbf{a}_1} \\ 0 & 0 & -ie^{-i\mathbf{k}\cdot\mathbf{a}_1} & 0 \end{pmatrix} \mathbf{S}_{\mathbf{k}} \mathbf{A}_{\mathbf{k}},$$

$$\sigma_{\mathbf{r}}^x \sigma_{\mathbf{r}+\mathbf{M_3}}^x \rightarrow \mathbf{A}_{-\mathbf{q}-\mathbf{k}}^{\mathbf{T}} \mathbf{S}_{\mathbf{k}}^\dagger \begin{pmatrix} 0 & -i & 0 & 0 \\ i & 0 & 0 & 0 \\ 0 & 0 & 0 & 0 \\ 0 & 0 & 0 & 0 \end{pmatrix} \mathbf{S}_{\mathbf{k}} \mathbf{A}_{\mathbf{k}}, \quad \sigma_{\mathbf{r}}^x \sigma_{\mathbf{r}+\mathbf{M_4}}^x \rightarrow \mathbf{A}_{-\mathbf{q}-\mathbf{k}}^{\mathbf{T}} \mathbf{S}_{\mathbf{k}}^\dagger \begin{pmatrix} 0 & 0 & 0 & 0 \\ 0 & 0 & 0 & 0 \\ 0 & 0 & 0 & ie^{i\mathbf{k}\cdot\mathbf{a}_2} \\ 0 & 0 & -ie^{-i\mathbf{k}\cdot\mathbf{a}_2} & 0 \end{pmatrix} \mathbf{S}_{\mathbf{k}} \mathbf{A}_{\mathbf{k}},$$

$$\sigma_{\mathbf{r}}^z \sigma_{\mathbf{r}+\mathbf{M_5}}^z \rightarrow \mathbf{A}_{-\mathbf{q}-\mathbf{k}}^{\mathbf{T}} \mathbf{S}_{\mathbf{k}}^\dagger \begin{pmatrix} 0 & 0 & -i & 0 \\ 0 & 0 & 0 & i \\ i & 0 & 0 & 0 \\ 0 & -i & 0 & 0 \end{pmatrix} \mathbf{S}_{\mathbf{k}} \mathbf{A}_{\mathbf{k}}, \quad (24)$$

where $\mathbf{a}_i$ are the primitive unit vectors, $S_{\mathbf{k}} = diag\{\exp i\mathbf{k}\cdot\mathbf{r_j}\}_{j=c,b,d,a}$ and

$$\mathbf{A}_{-\mathbf{q}-\mathbf{k}}^{\mathbf{T}} = \begin{pmatrix} c_{-\mathbf{q}-\mathbf{k}} \\ b_{-\mathbf{q}-\mathbf{k}} \\ d_{-\mathbf{q}-\mathbf{k}} \\ a_{-\mathbf{q}-\mathbf{k}} \end{pmatrix}^{\mathbf{T}}, \quad \mathbf{A_k} = \begin{pmatrix} c_{\mathbf{k}} \\ b_{\mathbf{k}} \\ d_{\mathbf{k}} \\ a_{\mathbf{k}} \end{pmatrix},$$

where in order to have simpler notations we denoted $c_{\mathbf{k},A} \equiv a_{\mathbf{k}}$, $c_{\mathbf{k},B} \equiv b_{\mathbf{k}}$, $c_{\mathbf{k},C} \equiv c_{\mathbf{k}}$, $c_{\mathbf{k},D} \equiv d_{\mathbf{k}}$. We used this particular order in forming the vector of the Majorana fermions, because we would like to use the auxiliary Pauli matrices for the spin products entering in Eq. (24). Next we perform the Fourier transformation of the strain tensor into the momentum space: $\epsilon_{\alpha\beta}(\mathbf{r}) = \frac{1}{\sqrt{N}} \times \sum_{\mathbf{q}} \frac{i}{2}(q_\alpha u_{\mathbf{q},\beta} + q_\beta u_{\mathbf{q},\alpha})$. We can now rewrite the Majorana-phonon coupling Hamiltonian as a sum of the contributions from different symmetry channels:

$$\mathcal{H}_c = \sqrt{\frac{2}{N}} \sum_{\mathbf{k},\mathbf{q}} \left(\mathcal{H}_{\mathbf{k},\mathbf{q}}^{A_g} + \mathcal{H}_{\mathbf{k},\mathbf{q}}^{B_{1g}} + \mathcal{H}_{\mathbf{k},\mathbf{q}}^{B_{2g}} + \mathcal{H}_{\mathbf{k},\mathbf{q}}^{B_{3g}} \right), \quad (25)$$

with

$$\mathcal{H}_{\mathbf{q},\mathbf{k}}^{A_g} = i\lambda_{A_g}(4q_c u_{\mathbf{q},c}\mathbf{A}_{-\mathbf{q}-\mathbf{k}}^{\mathbf{T}}\mathbf{S}_{\mathbf{k}}^\dagger \begin{pmatrix} \hat{O} & -i\hat{\sigma}_3 \\ i\hat{\sigma}_3 & \hat{O} \end{pmatrix} \mathbf{S_k}\mathbf{A_k} +$$
$$+ \left(q_c u_{\mathbf{q},c} + 2q_b u_{\mathbf{q},b} + q_a u_{\mathbf{q},a}\right)\mathbf{A}_{-\mathbf{q}-\mathbf{k}}^{\mathbf{T}}\mathbf{S}_{\mathbf{k}}^\dagger \hat{Q}_{\mathbf{k},1}\mathbf{S_k}\mathbf{A_k}),$$

$$\mathcal{H}_{\mathbf{q},\mathbf{k}}^{B_{1g}} = \frac{i\lambda_{B_{1g}}}{2}\left(q_a u_{\mathbf{q},b} + q_b u_{\mathbf{q},a}\right)\mathbf{A}_{-\mathbf{q}-\mathbf{k}}^{\mathbf{T}}\mathbf{S}_{\mathbf{k}}^\dagger \hat{Q}_{\mathbf{k},2}\mathbf{S_k}\mathbf{A_k}, \quad (26)$$

$$\mathcal{H}_{\mathbf{q},\mathbf{k}}^{B_{2g}} = \frac{i\lambda_{B_{2g}}}{2}\left(q_a u_{\mathbf{q},c} + q_c u_{\mathbf{q},a}\right)\mathbf{A}_{-\mathbf{q}-\mathbf{k}}^{\mathbf{T}}\mathbf{S}_{\mathbf{k}}^\dagger \hat{Q}_{\mathbf{k},3}\mathbf{S_k}\mathbf{A_k},$$

$$\mathcal{H}_{\mathbf{q},\mathbf{k}}^{B_{3g}} = \frac{i\lambda_{B_{3g}}}{2}\left(q_b u_{\mathbf{q},c} + q_c u_{\mathbf{q},b}\right)\mathbf{A}_{-\mathbf{q}-\mathbf{k}}^{\mathbf{T}}\mathbf{S}_{\mathbf{k}}^\dagger \hat{Q}_{\mathbf{k},4}\mathbf{S_k}\mathbf{A_k}.$$

Here we denote $\hat{O} = \begin{pmatrix} 0 & 0 \\ 0 & 0 \end{pmatrix}$, $\hat{\sigma}_i$ are the auxiliary Pauli matrices and $\hat{Q}_{\mathbf{k}}$-matrices are defined as

$$\hat{Q}_{\mathbf{k},1} = \begin{pmatrix} [1+\cos(\mathbf{k}\cdot\mathbf{a}_3)]\hat{\sigma}_2 + \sin(\mathbf{k}\cdot\mathbf{a}_3)\hat{\sigma}_1 & \hat{O} \\ \hat{O} & -[\cos(\mathbf{k}\cdot\mathbf{a}_1)+\cos(\mathbf{k}\cdot\mathbf{a}_2)]\hat{\sigma}_2 - [\sin(\mathbf{k}\cdot\mathbf{a}_1)+\sin(\mathbf{k}\cdot\mathbf{a}_2)]\hat{\sigma}_1 \end{pmatrix},$$

$$\hat{Q}_{\mathbf{k},2} = \begin{pmatrix} [1+\cos(\mathbf{k}\cdot\mathbf{a}_3)]\hat{\sigma}_2 + \sin(\mathbf{k}\cdot\mathbf{a}_3)\hat{\sigma}_1 & \hat{O} \\ \hat{O} & [\cos(\mathbf{k}\cdot\mathbf{a}_1)+\cos(\mathbf{k}\cdot\mathbf{a}_2)]\hat{\sigma}_2 + [\sin(\mathbf{k}\cdot\mathbf{a}_1)+\sin(\mathbf{k}\cdot\mathbf{a}_2)]\hat{\sigma}_1 \end{pmatrix}, \quad (27)$$

$$\hat{Q}_{\mathbf{k},3} = \begin{pmatrix} [1-\cos(\mathbf{k}\cdot\mathbf{a}_3)]\hat{\sigma}_2 - \sin(\mathbf{k}\cdot\mathbf{a}_3)\hat{\sigma}_1 & \hat{O} \\ \hat{O} & [\cos(\mathbf{k}\cdot\mathbf{a}_1)-\cos(\mathbf{k}\cdot\mathbf{a}_2)]\hat{\sigma}_2 + [\sin(\mathbf{k}\cdot\mathbf{a}_1)-\sin(\mathbf{k}\cdot\mathbf{a}_2)]\hat{\sigma}_1 \end{pmatrix},$$

$$\hat{Q}_{\mathbf{k},4} = \begin{pmatrix} [1-\cos(\mathbf{k}\cdot\mathbf{a}_3)]\hat{\sigma}_2 - \sin(\mathbf{k}\cdot\mathbf{a}_3)\hat{\sigma}_1 & \hat{O} \\ \hat{O} & [\cos(\mathbf{k}\cdot\mathbf{a}_2)-\cos(\mathbf{k}\cdot\mathbf{a}_1)]\hat{\sigma}_2 + [\sin(\mathbf{k}\cdot\mathbf{a}_2)-\sin(\mathbf{k}\cdot\mathbf{a}_1)]\hat{\sigma}_1 \end{pmatrix}.$$

Note also that since we are using the long wavelength limit for the phonons, we only kept the leading in $\mathbf{q}$ terms in all the expressions.

To obtain the expressions for the MFPh coupling vertices, we express the phonon modes in terms of the transverse/longitudinal eigenmodes (12) and get

$$\mathcal{H}_{\mathbf{q},\mathbf{k}}^{\parallel} = \tilde{u}_{\mathbf{q}}^{\parallel}\mathbf{A}_{-\mathbf{q}-\mathbf{k}}\mathbf{S}_{\mathbf{k}}^\dagger \hat{\lambda}_{\mathbf{q},\mathbf{k}}^{\parallel}\mathbf{S_k}\mathbf{A_k},$$

$$\mathcal{H}_{\mathbf{q},\mathbf{k}}^{1,\perp} = \tilde{u}_{\mathbf{q}}^{1,\perp}\mathbf{A}_{-\mathbf{q}-\mathbf{k}}\mathbf{S}_{\mathbf{k}}^\dagger \hat{\lambda}_{\mathbf{q},\mathbf{k}}^{1,\perp}\mathbf{S_k}\mathbf{A_k}, \quad (28)$$

$$\mathcal{H}_{\mathbf{q},\mathbf{k}}^{2,\perp} = \tilde{u}_{\mathbf{q}}^{1,\perp}\mathbf{A}_{-\mathbf{q}-\mathbf{k}}\mathbf{S}_{\mathbf{k}}^\dagger \hat{\lambda}_{\mathbf{q},\mathbf{k}}^{2,\perp}\mathbf{S_k}\mathbf{A_k},$$

where the MFPh vertices are given by

$$\hat{\lambda}_{\mathbf{q},\mathbf{k}}^{\parallel} = i\lambda_{A_g}\left(4q_c R_{31}\begin{pmatrix} \hat{O} & -i\hat{\sigma}_3 \\ i\hat{\sigma}_3 & \hat{O} \end{pmatrix} + (q_c R_{31} + 2q_b R_{21} + q_a R_{11})\hat{Q}_{\mathbf{k},1}\right) +$$

$$+ \frac{i\lambda_{B_{1g}}}{2}(q_a R_{21} + q_b R_{11})\hat{Q}_{\mathbf{k},2} + \frac{i\lambda_{B_{2g}}}{2}(q_a R_{31} + q_c R_{11})\hat{Q}_{\mathbf{k},3} + \frac{i\lambda_{B_{3g}}}{2}(q_b R_{31} + q_c R_{21})\hat{Q}_{\mathbf{k},4},$$

$$\hat{\lambda}_{\mathbf{q,k}}^{1,\perp} = i\lambda_{A_g}\left(4q_c R_{32}\begin{pmatrix}\hat{O} & -i\hat{\sigma}_3 \\ i\hat{\sigma}_3 & \hat{O}\end{pmatrix} + (q_c R_{32} + 2q_b R_{22} + q_a R_{12})\hat{Q}_{\mathbf{k},1}\right) +$$

$$+\frac{i\lambda_{B_{1g}}}{2}(q_a R_{22} + q_b R_{12})\hat{Q}_{\mathbf{k},2} + \frac{i\lambda_{B_{2g}}}{2}(q_a R_{32} + q_c R_{12})\hat{Q}_{\mathbf{k},3} + \frac{i\lambda_{B_{3g}}}{2}(q_b R_{32} + q_c R_{22})\hat{Q}_{\mathbf{k},4},$$

$$\hat{\lambda}_{\mathbf{q,k}}^{2,\perp} = i\lambda_{A_g}\left(4q_c R_{33}\begin{pmatrix}\hat{O} & -i\hat{\sigma}_3 \\ i\hat{\sigma}_3 & \hat{O}\end{pmatrix} + (q_c R_{33} + 2q_b R_{23} + q_a R_{13})\hat{Q}_{\mathbf{k},1}\right) +$$

$$+\frac{i\lambda_{B_{1g}}}{2}(q_a R_{23} + q_b R_{13})\hat{Q}_{\mathbf{k},2} + \frac{i\lambda_{B_{2g}}}{2}(q_a R_{33} + q_c R_{13})\hat{Q}_{\mathbf{k},3} + \frac{i\lambda_{B_{3g}}}{2}(q_b R_{33} + q_c R_{23})\hat{Q}_{\mathbf{k},4}. \tag{29}$$

4. Summary

In this work, we perform the first step in the study of the phonon dynamics in the Kitaev model on the hyperhoneycomb and derive the Majorana fermion-phonon coupling vertices using the symmetry considerations. We will use these vertices to compute phonon attenuation, phonon conductivity, phonon viscosity, and phonon Hall effect, which indirectly will allow us to study the fractionalized excitations in the Kitaev spin liquid. The latter two observables are non-zero only in the presence of time-reversal symmetry breaking due to applying a magnetic field.

All these observables can be obtained from the phonon self-energy (17), this diagrammatic computation procedure was formulated by some of us in Refs. 20, 21. In particular, the sound attenuation is determined by the decay of a phonon into a pair of Majorana fermions and can be calculated from the imaginary part of the phonon self-energy as

$$\alpha_s(\mathbf{q}) \sim -\frac{1}{v_s^2 q}\text{Im}\Big[\Pi_{\text{ph}}(\mathbf{q},\Omega)\Big]_{\Omega = v_s|q|}, \tag{30}$$

where v_s is the sound velocity, which in our case depends on the direction of $\mathbf{q}$. We expect that the attenuation rate due to this process will be linear in temperature due to the vanishing density of states at the vicinity of the nodal line and, thus, will be the dominant one compared with the sound attenuation due to phonon-phonon interactions that in the three-dimensional system scales as $\propto T^4$. Our preliminary results, which will be published elsewhere, indicate that due to the presence of the nodal line in the low-energy Majorana fermion spectrum, the scattering of the acoustic phonons on the Majorana fermions is stronger for the hyperhoneycomb lattice than for the honeycomb lattice. The sound attenuation also shows a strong angular dependence at the leading order in phonon momentum q since both the sound velocity on the hyperhoneycomb lattice and the Fermi velocity of the low-energy Majorana fermions strongly depends on the spatial direction. We also anticipate that the Z_2 fluxes will play an important role in the phonon dynamics at temperatures above the flux gap. Finally, the same Majorana fermion-phonon interaction also gives rise

to the finite lifetime of the Majorana fermions. This effect, however, is quite weak, and the lifetime scales as $\tau_f \sim T^2$, which is much smaller than the typical fermion energy $\sim T$.

Acknowledgments

_____

1. P. A. Lee, *Science* **321**, 1306 (2008).

2. L. Balents, *Nature* **464**, 199 (2010).

3. L. Savary and L. Balents, *Rep. Prog. Phys.* **80**, 016502 (2017).

4. Y. Zhou, K. Kanoda, and T.-K. Ng, *Rev. Mod. Phys.* **89**, 025003 (2017).

5. J. Knolle and R. Moessner, *Annu. Rev. Condens. Matter Phys.* **10**, 451 (2019).

6. C. Broholm, R. J. Cava, S. A. Kivelson, D. G. Nocera, M. R. Norman, and T. Senthil, *Science* **367** (2020).

7. Y. Motome and J. Nasu, *J. Phys. Soc. Jpn.* **89**, 012002 (2020).

8. S. Yamashita, Y. Nakazawa, M. Oguni, Y. Oshima, H. Nojiri, Y. Shimizu, K. Miyagawa, and K. Kanoda, *Nature Phys.* **4**, 459 (2008).

9. Y. Shimizu, K. Miyagawa, K. Kanoda, M. Maesato, and G. Saito, *Phys. Rev. Lett.* **91**, 107001 (2003).

10. T. Itou, A. Oyamada, S. Maegawa, M. Tamura, and R. Kato, *Phys. Rev. B* **77**, 104413 (2008).

11. M. Yamashita, N. Nakata, Y. Senshu, M. Nagata, H. M. Yamamoto, R. Kato, T. Shibauchi, and Y. Matsuda, *Science* **328**, 1246 (2010).

12. H. D. Zhou, E. S. Choi, G. Li, L. Balicas, C. R. Wiebe, Y. Qiu, J. R. D. Copley, and J. S. Gardner, *Phys. Rev. Lett.* **106**, 147204 (2011).

13. B. Fåk, E. Kermarrec, L. Messio, B. Bernu, C. Lhuillier, F. Bert, P. Mendels, B. Koteswararao, F. Bouquet, J. Ollivier, A. D. Hillier, A. Amato, R. H. Colman, and A. S. Wills, *Phys. Rev. Lett.* **109**, 037208 (2012).

14. Y. Okamoto, M. Nohara, H. Aruga-Katori, and H. Takagi, *Phys. Rev. Lett.* **99**, 137207 (2007).

15. H. Takagi, T. Takayama, G. Jackeli, G. Khaliullin, and S. E. Nagler, *Nat. Rev. Phys.* **1**, 264 (2019).

16. A. A. Tsirlin and P. Gegenwart, *arXiv:2103.14073* (2021).

17. Y. Zhou and P. A. Lee, *Phys. Rev. Lett.* **106**, 056402 (2011).

18. M. Serbyn and P. A. Lee, *Phys. Rev. B* **87**, 174424 (2013).

19. A. Metavitsiadis and W. Brenig, *Phys. Rev. B* **101**, 035103 (2020).

20. M. Ye, R. M. Fernandes, and N. B. Perkins, *Phys. Rev. Res.* **2**, 033180 (2020).

21. K. Feng, M. Ye, and N. B. Perkins, *Phys. Rev. B* **103**, 214416 (2021).

22. A. Metavitsiadis, W. Natori, J. Knolle, and W. Brenig, *arXiv:2103.09828* (2021).

23. R. Hentrich, A. U. B. Wolter, X. Zotos, W. Brenig, D. Nowak, A. Isaeva, T. Doert, A. Banerjee, P. Lampen-Kelley, D. G. Mandrus, S. E. Nagler, J. Sears, Y.-J. Kim, B. Büchner, and C. Hess, *Phys. Rev. Lett.* **120**, 117204 (2018).

24. Y. Kasahara, T. Ohnishi, Y. Mizukami, O. Tanaka, S. Ma, K. Sugii, N. Kurita, H. Tanaka, J. Nasu, Y. Motome, T. Shibauchi, and Y. Matsuda, *Nature* **559**, 227 (2018).

25. S. Pal, A. Seth, P. Sakrikar, A. Ali, S. Bhattacharjee, D. V. S. Muthu, Y. Singh, and A. K. Sood, *arXiv:2011.00606* (2020).

26. H. Li, T. T. Zhang, A. Said, G. Fabbris, D. G. Mazzone, J. Q. Yan, D. Mandrus, G. B. Halasz, S. Okamoto, S. Murakami, M. P. M. Dean, H. N. Lee, and H. Miao, *arXiv:2011.07036* (2020).

27. L. J. Sandilands, Y. Tian, K. W. Plumb, Y.-J. Kim, and K. S. Burch, *Phys. Rev. Lett.* **114**, 147201 (2015).

28. A. Glamazda, P. Lemmens, S.-H. Do, Y. S. Kwon, and K.-Y. Choi, *Phys. Rev. B* **95**, 174429 (2017).

29. T. T. Mai, A. McCreary, P. Lampen-Kelley, N. Butch, J. R. Simpson, J.-Q. Yan, S. E. Nagler, D. Mandrus, A. R. H. Walker, and R. V. Aguilar, *Phys. Rev. B* **100**, 134419 (2019).

30. D. Wulferding, Y. Choi, S.-H. Do, C. H. Lee, P. Lemmens, C. Faugeras, Y. Gallais, and K.-Y. Choi, *Nat. Commun.* **11**, 1603 (2020).

31. D. Lin, K. Ran, H. Zheng, J. Xu, L. Gao, J. Wen, S.-L. Yu, J.-X. Li, and X. Xi, *Phys. Rev. B* **101**, 045419 (2020).

32. A. Kitaev, *Ann. Phys.* **321**, 2 (2006).

33. S. Mandal and N. Surendran, *Phys. Rev. B* **79**, 024426 (2009).

34. M. Hermanns and S. Trebst, *Phys. Rev. B* **89**, 235102 (2014).

35. M. Hermanns, K. O'Brien, and S. Trebst, *Phys. Rev. Lett.* **114**, 157202 (2015).

36. B. Perreault, J. Knolle, N. B. Perkins, and F. J. Burnell, *Phys. Rev. B* **92**, 094439 (2015).

37. B. Perreault, J. Knolle, N. B. Perkins, and F. J. Burnell, *Phys. Rev. B* **94**, 104427 (2016).

38. G. B. Halász, B. Perreault, and N. B. Perkins, *Phys. Rev. Lett.* **119**, 097202 (2017).

39. S. Trebst, *arXiv:1701.07056* (2017).

40. T. Eschmann, P. A. Mishchenko, K. O'Brien, T. A. Bojesen, Y. Kato, M. Hermanns, Y. Motome, and S. Trebst, *Phys. Rev. B* **102**, 075125 (2020).

41. G. Jackeli and G. Khaliullin, *Phys. Rev. Lett.* **102**, 017205 (2009).

42. J. Chaloupka, G. Jackeli, and G. Khaliullin, *Phys. Rev. Lett.* **105**, 027204 (2010).

43. Y. Singh and P. Gegenwart, *Phys. Rev. B* **82**, 064412 (2010).

44. Y. Singh, S. Manni, J. Reuther, T. Berlijn, R. Thomale, W. Ku, S. Trebst, and P. Gegenwart, *Phys. Rev. Lett.* **108**, 127203 (2012).

45. S. C. Williams, R. D. Johnson, F. Freund, S. Choi, A. Jesche, I. Kimchi, S. Manni, A. Bombardi, P. Manuel, P. Gegenwart, and R. Coldea, *Phys. Rev. B* **93**, 195158 (2016).

46. K. W. Plumb, J. P. Clancy, L. J. Sandilands, V. V. Shankar, Y. F. Hu, K. S. Burch, H.-Y. Kee, and Y.-J. Kim, *Phys. Rev. B* **90**, 041112 (2014).

47. J. A. Sears, M. Songvilay, K. W. Plumb, J. P. Clancy, Y. Qiu, Y. Zhao, D. Parshall, and Y.-J. Kim, *Phys. Rev. B* **91**, 144420 (2015).

48. A. Biffin, R. D. Johnson, I. Kimchi, R. Morris, A. Bombardi, J. G. Analytis, A. Vishwanath, and R. Coldea, *Phys. Rev. Lett.* **113**, 197201 (2014).

49. T. Takayama, A. Kato, R. Dinnebier, J. Nuss, H. Kono, L. S. I. Veiga, G. Fabbris, D. Haskel, and H. Takagi, *Phys. Rev. Lett.* **114**, 077202 (2015).

50. A. Biffin, R. D. Johnson, S. Choi, F. Freund, S. Manni, A. Bombardi, P. Manuel, P. Gegenwart, and R. Coldea, *Phys. Rev. B* **90**, 205116 (2014).

51. K. A. Modic, T. E. Smidt, I. Kimchi, N. P. Breznay, A. Biffin, S. Choi, R. D. Johnson, R. Coldea, P. Watkins-Curry, G. T. McCandess, *et al.*, *Nat. Commun.* **5**, 4203 (2014).

52. S. H. Chun, J.-W. Kim, J. Kim, H. Zheng, C. C. Stoumpos, C. Malliakas, J. Mitchell, K. Mehlawat, Y. Singh, Y. Choi, *et al.*, *Nat. Phys.* **11**, 462 (2015).

53. A. Banerjee, C. Bridges, J.-Q. Yan, A. Aczel, L. Li, M. Stone, G. Granroth, M. Lumsden, Y. Yiu, J. Knolle, *et al.*, *Nature Mater.* **15**, 733 (2016).

54. A. Banerjee, J. Yan, J. Knolle, C. A. Bridges, M. B. Stone, M. D. Lumsden, D. G. Mandrus, D. A. Tennant, R. Moessner, and S. E. Nagler, *Science* **356**, 1055 (2017).

55. S.-H. Baek, S.-H. Do, K.-Y. Choi, Y. S. Kwon, A. U. B. Wolter, S. Nishimoto, J. van den Brink, and B. Büchner, *Phys. Rev. Lett.* **119**, 037201 (2017).

56. M. Majumder, R. S. Manna, G. Simutis, J. C. Orain, T. Dey, F. Freund, A. Jesche, R. Khasanov, P. K. Biswas, E. Bykova, *et al.*, *Phys. Rev. Lett.* **120**, 237202 (2018).

57. L. S. I. Veiga, M. Etter, K. Glazyrin, F. Sun, C. A. Escanhoela, G. Fabbris, J. R. L. Mardegan, P. S. Malavi, Y. Deng, P. P. Stavropoulos, *et al.*, *Phys. Rev. B* **96**, 140402 (2017).

58. N. P. Breznay, A. Ruiz, A. Frano, W. Bi, R. J. Birgeneau, D. Haskel, and J. G. Analytis, *Phys. Rev. B* **96**, 020402 (2017).

59. T. Takayama, A. Krajewska, A. S. Gibbs, A. N. Yaresko, H. Ishii, H. Yamaoka, K. Ishii, N. Hiraoka, N. P. Funnell, C. L. Bull, *et al.*, *Phys. Rev. B* **99**, 125127 (2019).

60. A. Ruiz, N. P. Breznay, M. Li, I. Rousochatzakis, A. Allen, I. Zinda, V. Nagarajan, G. Lopez, Upton, J. Kim, *et al.*, *arXiv:2102.02714v2 [cond-mat.str-el] 5 Feb 2021*.

61. J. Knolle, D. L. Kovrizhin, J. T. Chalker, and R. Moessner, *Phys. Rev. Lett.* **112**, 207203 (2014).

62. J. Knolle, G.-W. Chern, D. L. Kovrizhin, R. Moessner, and N. B. Perkins, *Phys. Rev. Lett.* **113**, 187201 (2014).

63. J. Knolle, D. L. Kovrizhin, J. T. Chalker, and R. Moessner, *Phys. Rev. B* **92**, 115127 (2015).

64. A. Smith, J. Knolle, D. L. Kovrizhin, J. T. Chalker, and R. Moessner, *Phys. Rev. B* **93**, 235146 (2016).

65. G. B. Halász, N. B. Perkins, and J. van den Brink, *Phys. Rev. Lett.* **117**, 127203 (2016).

66. G. B. Halász, S. Kourtis, J. Knolle, and N. B. Perkins, *Phys. Rev. B* **99**, 184417 (2019).

67. E. H. Lieb, *Phys. Rev. Lett.* **73**, 2158 (1994).

68. F. L. Pedrocchi, S. Chesi, and D. Loss, *Phys. Rev. B* **84**, 165414 (2011).

69. L. D. Landau, L. P. Pitaevskii, A. M. Kosevich, and E. M. Lifshitz, *Theory of Elasticity*, Butterworth-Heinemann, 3rd edition (2012).

70. From private communications with Alexander Tsirlin, the non-zero elastic modulus tensor coeficients in β-LiIr$_2$O$_3$ (in kbar) are C_{aaaa} = 2848:9530, C_{bbbb} =2636:5278, C_{cccc} = 2658:3422, C_{aabb} = 881:9877, C_{aacc} =1273:9659, C_{bbcc} = 1177:4125, C_{aabb} = 881:9877, C_{abab} =814:5967, C_{acac} = 903:3235, C_{bcbc} = 704:7004.

71. N. Ashcroft and N. Mermin, *Solid State Physics*, HRW International Editions, Holt, Rinehart and Winston (1976).

———————————————

Магнітопружні ефекти у гіперсотовій спіновій китаєвській рідині

Aysel Shiralieva, Artem Prokoshin, Natalia B. Perkins

В останні роки припускалося, що декілька моттовських ізоляторів з великою спін-орбітальною взаємодією можуть бути близькими до квантової спінової рідини Китаєва, цікавою особливістю якої є розподіл спінових збуджень на рухомі ферміони Майорани та статичні Z_2 потоки. На жаль, основний стан цих систем важко зафіксувати експериментально, бо він не виявляє особливостей на відміну від звичайного локального зондування. Запропоновано для знаходження проявів розділення збуджень використовувати їхній зв'язок із коливаннями гратки, тобто магнітопружний зв'язок, який виникає внаслідок залежності взаємодії між спінами від їхньої відносної відстані. Показано, що магнітопружний зв'язок може приводити до суттєвих модифікацій фононної динаміки, яка може спостерігатися у вигляді перенормування вимірюваного фононного спектра, загасання звуку та холлівської фононної в'язкості. Це робить фононну динаміку перспективним інструментом для характеризування та ідентифікації фаз квантової спінової рідини. Основну увагу приділено магнітопружним ефектам у тривимірній моделі Китаєва, яка реалізується у гіперсотовій гратці. Гіперсотова китаєвська спінова рідина дуже цікава, бо сильну китаєвську взаємодію було спостережено у китаєвському магнетику β-Li$_2$IrO$_3$, в якому спін-орбітально пов'язані J_{eff} = 1/2 моменти іридію формують точну гіперсотову гратку.

Ключові слова: фононна динаміка, магнітопружний зв'язок, квантова спінова рідина.